6-15-2022

# Multifunctional Hybrid MoS2-PEGylated/Au Nanostructures with Potential Theranostic Applications in Biomedicine

Thiago R. S. Malagrino

Anna Paula Godoy

Juliano M. Barbosa

Abner G. T. Lima

Nei C. O. Sousa

*See next page for additional authors*



## Recommended Citation

Malagrino, T.R.S.; Godoy, A.P.; Barbosa, J.M.; Lima, A.G.T.; Sousa, N.C.O.; Pedrotti, J.J.; Garcia, P.S.; Paniago, R.M.; Andrade, L.M.; Domingues, S.H.; Silva, W.M.; Ribeiro, H.; Taha-Tijerina, J. Multifunctional Hybrid MoS2-PEGylated/Au Nanostructures with Potential Theranostic Applications in Biomedicine. Nanomaterials 2022, 12, 2053. https://doi.org/10.3390/nano12122053

*nanomaterials*

MDPI

*Article*

# Multifunctional Hybrid $MoS_2$-PEGylated/Au Nanostructures with Potential Theranostic Applications in Biomedicine

**Thiago R. S. Malagrino [1], Anna P. Godoy [1], Juliano M. Barbosa [1], Abner G. T. Lima [1], Nei C. O. Sousa [1], Jairo J. Pedrotti [1], Pamela S. Garcia [1], Roberto M. Paniago [2], Lídia M. Andrade [2], Sergio H. Domingues [1,3], Wellington M. Silva [4], Hélio Ribeiro [1] and Jaime Taha-Tijerina [5,6,*]**

1 Engineering School, Mackenzie Presbyterian University, Rua da Consolação 896, São Paulo 01302-907, SP, Brazil; thiago.malagrino@hotmail.com (T.R.S.M.); annapsgodoy@hotmail.com (A.P.G.); juliano.barbosa@mackenzie.br (J.M.B.); abn.guilherme@gmail.com (A.G.T.L.); nei.sousa@mackenzie.br (N.C.O.S.); jairojpedrotti@gmail.com (J.J.P.); pamela.s.garcia@gmail.com (P.S.G.); sergio.domingues@mackenzie.br (S.H.D.); helio.ribeiro1@mackenzie.br (H.R.)

2 Departamento de Física, Universidade Federal de Minas Gerais, Avenida Presidente Antônio Carlos, 6.627, Belo Horizonte 31270-901, MG, Brazil; paniago@fisica.ufmg.br (R.M.P.); lidia.nanobmrg@gmail.com (L.M.A.)

3 MackGraphe, Mackenzie Institute for Advanced Research in Graphene and Nanotechnologies, Rua da Consolação 896, São Paulo 01302-907, SP, Brazil

4 Departamento de Química, Universidade Federal de Minas Gerais, Avenida Presidente Antônio Carlos, 6.627, Belo Horizonte 31270-901, MG, Brazil; wellingtonmarcos@yahoo.com.br

5 Engineering Department, Universidad de Monterrey, Av. Ignacio Morones Prieto 4500 Pte., San Pedro Garza García 66238, NL, Mexico

6 Engineering Technology Department, University of Texas Rio Grande Valley, Brownsville, TX 78520, USA

* Correspondence: jose.taha@udem.edu

**Abstract:** In this work, flower-like molybdenum disulfide ($MoS_2$) microspheres were produced with polyethylene glycol (PEG) to form $MoS_2$-PEG. Likewise, gold nanoparticles (AuNPs) were added to form $MoS_2$-PEG/Au to investigate its potential application as a theranostic nanomaterial. These nanomaterials were fully characterized by scanning electron microscopy (SEM), transmission electron microscopy (TEM), X-ray diffraction (XRD), photoelectron X-ray spectroscopy (XPS), Fourier-transformed infrared spectroscopy (FTIR), cyclic voltammetry and impedance spectroscopy. The produced hierarchical $MoS_2$-PEG/Au microstructures showed an average diameter of 400 nm containing distributed gold nanoparticles, with great cellular viability on tumoral and non-tumoral cells. This aspect makes them with multifunctional characteristics with potential application for cancer diagnosis and therapy. Through the complete morphological and physicochemical characterization, it was possible to observe that both $MoS_2$-PEG and $MoS_2$-PEG/Au showed good chemical stability and demonstrated noninterference in the pattern of the cell nucleus, as well. Thus, our results suggest the possible application of these hybrid nanomaterials can be immensely explored for theranostic proposals in biomedicine.

**Keywords:** nanotechnology; hybrid nanostructures; molybdenum disulfide; PEGylated $MoS_2$; gold nanoparticles; theranostic; biocompatible

check for updates

**Citation:** Malagrino, T.R.S.; Godoy, A.P.; Barbosa, J.M.; Lima, A.G.T.; Sousa, N.C.O.; Pedrotti, J.J.; Garcia, P.S.; Paniago, R.M.; Andrade, L.M.; Domingues, S.H.; et al. Multifunctional Hybrid $MoS_2$-PEGylated/Au Nanostructures with Potential Theranostic Applications in Biomedicine. *Nanomaterials* **2022**, *12*, 2053. https://doi.org/10.3390/nano12122053

Academic Editor: Run Zhang

Received: 17 May 2022
Accepted: 9 June 2022
Published: 15 June 2022



## 1. Introduction

Over the last decades the application of nanomaterials in biomedicine has been raised, especially for biosensing and drug delivery. However, the main feature that must be considered to a given material be used in biomedical proposals is its physicochemical stability and biological safety [1]. In this context, molybdenum disulfide ($MoS_2$) and its derivatives have attracted attention due to its excellent biocompatibility and simple synthesis [2]. The 2D nanomaterials have been used in the diagnosis and therapy of cancer [3] especially when they are combined with gold nanoparticles [4–7]. For instance, graphene

and other nanocarbons [3,8,9], hexagonal boron nitride (h-BN) [1,10], black phosphorus (BP) [11], tungsten sulfide ($WS_2$) [12], molybdenum disulfide ($MoS_2$) [13–15], among others, have gained prominence mainly due to their huge biological applications [13]. Molybdenum disulfide is an important material because, in addition to being widely studied for use in cancer treatment [16,17], such as the photodynamic (PDT) and the photothermal (PTT) therapies, it is an abundant material with appreciated mechanical, thermal and electrical properties, that makes it also economically accessible [18,19]. Although $MoS_2$ is considered naturally biocompatible [20], it is common to seek an improvement in its colloidal stability for in vivo studies to achieve an increased penetration and dispersibility in the tissues of interest [13,21]. In some cases, the biochemical stability is reached by the modification of its surface, for instance with polyethylene glycol (PEG) as well as other chemical groups [5,6,13,16,22,23]. This functionalization process can allow its selectivity and effectiveness treatment in cancer cells promoting, for example localized and controlled hyperthermia by near-infrared radiation (NIR) [24,25]. It has the potential to replace conventional treatments such as chemotherapy [17]. Due to the ability of $MoS_2$ to convert light-to-heat its photothermal properties have been studied for cancer treatment, alone or in combination with different therapies [26]. For instance, an in vivo study that used human breast cancer xenograft model in nude mice, treated with PEGylated nanocubes containing $Fe_3O_4$@$MoS_2$ and Doxorubicin for MRI-guided chemo-photothermal therapy showed decreased tumor volume after 24 h of injection [27]. Shi et al. observed in MCF-7, a human breast cancer cell line, an increased apoptosis death due to the ability of $MoS_2$-PEG functionalized with Doxorubicin to evade endosomes via NIR light irradiation [28]. In the same way, AuNPs also are the most used element for nanoparticles-based biomedicine applications. One example is its fluorescence signals enhancement used for diagnostic purpose [29]. To our knowledge, there are few studies that report the use of $MoS_2$-PEG/Au for theranostic applications [30], reported in the literature, despite the significant advances in nanomaterials science applied in cancer diagnosis and therapy [5,13,17,23,26,31,32]. The use of hybrid nanostructures still lacks intense exploration in this specific area. In this work, hierarchical flower-like $MoS_2$-PEG or $MoS_2$-PEG/Au were produced and fully characterized. Moreover, the impact of these nanomaterials in the cellular viability was investigated in vitro and data show non-toxicity associated with both, suggesting their potential application in biomedicine.

## 2. Materials and Methods

### *2.1. Materials*

#### 2.1.1. Reagents

The reagents, ammonium molybdate, $(NH_4)_6Mo_7O_{24}$ (99.98%), Polyethylene glycol 20,000, $CH_3O(CH_2CH_2O)nCH_3$ (PEG-2000), Thioacetamide, $C_2H_5NS$ (98%), Ethanol, $C_2H_5OH$ (99.98%), acetone, $C_3H_6O$ (99.98%), Sodium borohydride, $NaBH_4$ (98%), Hexadecyltrimethylammonium bromide, $C_{19}H_{42}BrN$ (CTAB, 99%), Silver nitrate, $AgNO_3$ (99%), Gold (III) chloride trihydrate, $HAuCl_4 \cdot 3H_2O$ (99.99%), L-ascorbic acid and $C_6H_8O_6$ (99%), were obtained from Sigma Aldrich, Brazil.

All aqueous solutions were prepared with ultrapure water (resistivity > 18.2 MΩ.cm) generated by a Millipore Milli-Q system.

#### 2.1.2. Cell Lines and Reagents

All cell lines used (human squamous cell carcinoma A431, human pharynx carci-noma FaDU and green monkey kidney Vero CCL-81) were obtained from ATCC (Manas-sas, VA, USA) and grown at 37 °C with 90% humidity and 5% $CO_2$ incubator in DMEM High Glucose containing 1 mM sodium pyruvate from Gibco (Grand Island, NY, USA); they were also supplemented with 5% Fetal bovine serum from LGC Biotechnology (Cotia, SP, Brazil).

Trypsin solution from Gibco (New York, NY, USA). Hoechst 33,342 was obtained from Sigma Aldrich (New York, NY, USA). T25 Tissue culture flasks and multi-well plates were

obtained from Kasvi (Curitiba, PR, Brazil) and TPP (Trasadingen, Switzerland). Resazurin viability kit was purchased from Sigma (St. Louis, MO, USA).

### *2.2. Methods*

#### 2.2.1. $MoS_2$-PEG Synthesis

The material was synthesized with hydrothermal method. In a typical experiment, ammonium molybdate (1.80 g) and PEG-2000 (1.0 g) were dissolved in 60 mL deionized water under stirring. Thioacetamide (1.80 g) was added into the solution and the mixture was stirred for 1 h. Then the mixture was transferred into a 100 mL autoclave and reacted for 3 h at 180 °C in an oven. After the autoclave cooling, the precipitate was collected by filtration and washed several times with Milli-Q water, ethanol and acetone. The material was dried in an oven at 100 °C for 4 h and $MoS_2$ microspheres were obtained.

#### 2.2.2. Au Nanoparticles Production

The production of the gold nanoparticles (AuNPs) followed the method described by Meireles et al. [33]. The stock solution was prepared by mixing 5 mL of CTAB (0.2 M) and 5 mL of $HAuCl_4 \cdot 3H_2O$ (0.0005 M). Then, 60 µL of ice-cold $NaBH_4$ (0.010 M) was added to the mixture, resulting in a brownish-yellow solution. Vigorous stirring was kept for 2 min at room temperature. The growing solution was prepared by adding CTAB (0.20 M), $AgNO_3$ (0.02 M) and $HAuCl_4 \cdot 3H_2O$ (0.005 M). Then, 210 µL of L-ascorbic acid ($C_6H_8O_6$) (0.4 M) was added to the system as a moderate reducing agent changing the color of solution from brownish yellow to colorless. Finally, 300 µL of stock solution was added to the growing solution, kept stirring for 20 min, and gradually changing to a deep red color.

#### 2.2.3. $MoS_2$-PEG/Au Synthesis

The $MoS_2$ (500 mg) sample was dispersed in 70 mL of a mixture containing 350 mg of gold nanorods for 30 min in a bath ultrasound operating at power of 20 W. Then, the mixture was transferred for a polytetrafluoroethylene (PTFE) vessel. The reaction vessel was attached to an autoclave and the incorporation was carried out in an oven at a temperature of 180 °C for two hours.

#### 2.2.4. Sample Preparation for Electrical Measurements

For sheet resistance measurements and contact angle measurements $MoS_2$-PEG and $MoS_2$-PEG/Au samples were prepared by mechanical compaction using a Shimadzu, SSP-10 A, P/N 200–64,175 hydraulic. The materials were pressured at 50 kN for 2 min, which resulted in disks of 13 mm in diameter and 2 mm in thickness, which can be seen in Figure S2 in the Supporting Information. For electrochemical measurements flexible graphite sheets, 1 mm thick, were cut into 2 × 4 $cm^2$ rectangles which served as conductive substrate for the electrodes. The electrodes were prepared for use through a procedure that included cleaning the graphite surface with the aid of a soft paper and washing with 92% ethanol solution ($v/v$), followed by drying with $N_2$ flow. Then, around 1 $cm^2$ of the graphite electrodes were modified by drop-casting 1 mL dispersions (1.0 mg $mL^{-1}$) of $MoS_2$-PEG and $MoS_2$-PEG/Au in isopropyl alcohol. The samples were dried in an oven at 150 °C for 24 h.

#### 2.2.5. Cellular Viability Based on Resazurin Reduction Assay

Cellular viability was assessed by performing viability method according to the manufacturer's instructions (Sigma, St. Louis, MO, USA). Briefly, the cells were seeded at $1 \times 10^4$ cells per well in 96-well flat-bottom plates (Kasvi, Curitiba, PR, Brazil) and incubated for 24 h at 37 °C with 5% $CO_2$ atmosphere. Cells were exposed to four different concentrations of $MoS_2$-PEG and $MoS_2$-PEG/Au, respectively, 100 µg/mL, 50 µg/mL, 10 µg/mL and 5 µg/mL. For death control Triton 100 × 10% was used. Each sample was dispersed in ultrasonic bath for 60 min and left exposed to each cell line for 24 h and 48 h. Subsequently, 10 µL per well of the reagent resazurin were added to the cells already

cultured (1:10 final dilution). The cells were kept under biochemical reaction for 4 h at 37 °C in the dark and the absorbance at 580 nm was measured in a spectrophotometer (Multiskan GO, Thermo Fisher Scientific, Waltham, MA, USA). All tests were performed at least two times. The fraction of viable cells in treated groups was calculated as a percentage of the untreated control group that was considered 100% viable.

#### 2.2.6. Hoechst Nuclear Staining Assay

To evaluate cell death patterns after nanomaterials treatment, a fresh staining solution containing Hoechst 33,342 (5 μg/mL) was used. Briefly, $1 \times 10^4$ FaDU cells were seeded in a 96 well plate and after monolayer cell formation, cells were treated with 100 μg/mL of $MoS_2$-PEG/Au for 24 h and 48 h, respectively. Triton 100× was used as death control. Before staining, growth medium was removed and 50 μL of staining solution were added to each well. After 60 min at 37 °C, $CO_2$ incubator staining solution was removed and cells were fixed by formalin 10%. Cells were analyzed in an Evos FL cell image system microscope (Thermo Fischer, Waltham, MA, USA), (Belo Horizonte, Brazil). The stained cellular nuclei were counted by using ImageJ2 software (NIH, USA).

#### 2.2.7. Characterization

FTIR measurements were made with Thermo Nicolet 6700 equipment (São Paulo, Brazil). The spectra were collected in the ATR mode from 64 accumulations in the transmission mode and were adjusted, taking baseline corrections into account. Micro-Raman measurements were carried out using a Horiba Jobin Yvon iHR 550 spectrometer (São Paulo, Brazil). The 532.0 nm line of an Ar-Kr laser was used as the excitation source. UV–visible spectroscopy measurement of gold nanoparticles was carried out in a UV-2550 spectrometer (Shimadzu, Japan) (São Paulo, Brazil). The spectrum was collected from 1000 to 200 nm in water suspension, where more details can be seen in Figure S1b in the Supporting Information. SEM characterization was made in a Carl Zeiss Field Emission Scanning Electron Microscope, model sigma VP equipped with an energy-dispersive X-ray (EDS) (São Paulo, Brazil). EDS spectra were obtained using a Bunker detector 410-M and software Quantax Espirit 1.9 (São Paulo, Brazil). The Peakfit v4 program was used to adjust the EDS spectra. The STEM images were carried out on a FEI TECNAI G2 (São Paulo, Brazil), microscope with a tungsten filament electron gun of 200 kV. XPS spectra were obtained using monochromatic Al Kα radiation (1486.6 eV). XPS spectra were acquired at room temperature on a VG Scientific Escalab-220-ixL (Belo Horizonte, Brazil). The detailed states of the different elements (C1s, O1s, Mo3p, Mo3d and S2p and Au4f) were obtained from fitting the XPS peaks by using Lorentzian and Gaussian functions. The sheet resistance and electrical conductivity of the nanostructures were measured in quintuplicate at room temperature by using an Ossila T2001A2 Four-Point Probe System (Sheffield, UK) (São Paulo, Brazil), with a probe space of 1.27 mm. Each material was evaluated by the smallest current signal that showed any response as voltage output. The applied current was 5 μA for both samples. The electrochemical measurements were carried out with a potentiostat Metrohm, model PGSTAT 128N (São Paulo, Brazil), controlled by software NOVA version 1.1.1, combined with a lab-made cell with three-electrode configuration, shown in Figures S2 and S3 in the Supporting Information section.

## 3. Results and Discussion

*Characterization of Flower-Like $MoS_2$-PEG/Au*

The morphology and microstructure of the as-synthesized $MoS_2$ with polyethylene glycol (PEG) were characterized by SEM and STEM microscopy. SEM image (Figure 1a) shows that the structures are formed by uniform hierarchical microspheres of $MoS_2$ with average diameter of about 400 nm. According to the literature [34], PEG can provide template structure in the synthesis, obtaining flower-like $MoS_2$ microspheres. STEM images (Figure 2b,c) reveal that each microsphere is composed of several curled and ultra-thin nanosheets distributed on its surface, and the $MoS_2$ interlayer spacing has approximately 0.54 nm.

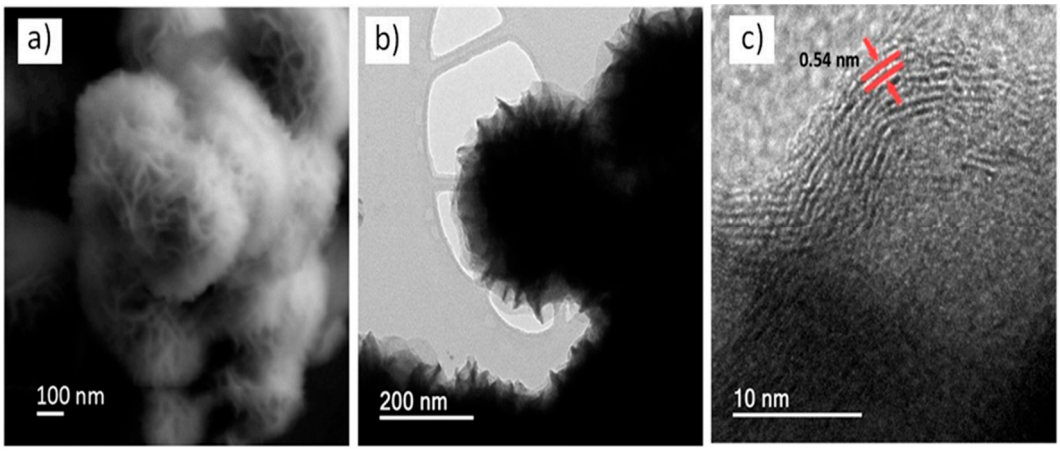


**Figure 1.** (**a**) SEM and (**b**,**c**) STEM images of the flower-like $MoS_2$ microspheres using PEG in the synthesis.

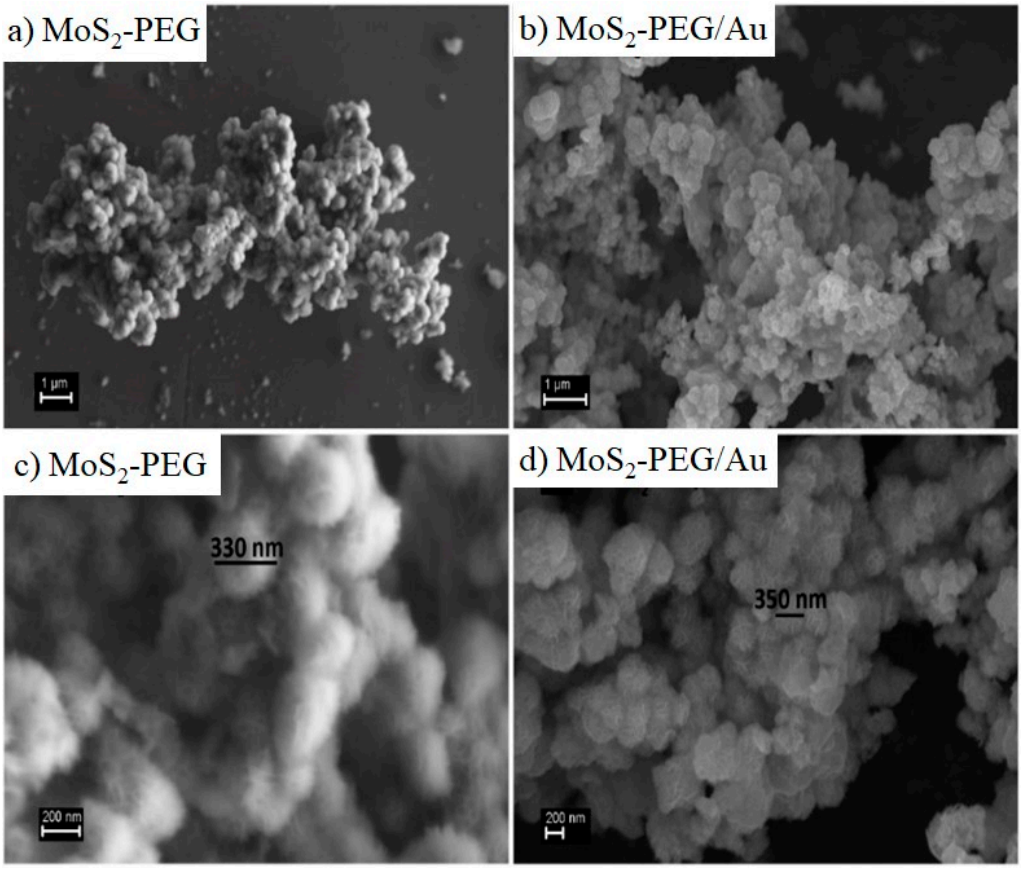


**Figure 2.** SEM images of the flower-like $MoS_2$ microspheres using: (**a**,**c**) PEG and (**b**,**d**) PEG/Au from their synthesis process.

Comparing the morphologies of the as-synthesized $MoS_2$-PEG (Figure 2a–c) and $MoS_2$PEG/Au by SEM (Figure 2b–d), it is noticeable that both structures appear as branched structure of aggregates with rough surface. However, when Au nanorods were added, microspheres exhibited less uniform shape showing a small difference in morphology in relation to the $MoS_2$-PEG (see Figure 2d).

Figure 3a–c shows EDS mapping were made to evaluate the element distribution of the $MoS_2$-PEG/Au sample. It can be observed that the elements Mo, S and Au are uniformly distributed in the studied area. The EDS spectrum (Figure 3d,e) reveals the dominance of Mo and the primary component of $MoS_2$, which is sulfur. The presence of C comes from

the PEG used as a "covering agent" of the nanoflake during the synthesis [35]. The peaks of Si and Al, which can be considered a type of impurity, are probably associated to the elements present in the sample holder. After modification with AuNPs (Figure 3e) a new peak referring to Au energy was identified [36]. Detailed discussion of the TEM and UV-vis of AuNPs can be seen in Figure S1 in Supporting Information.

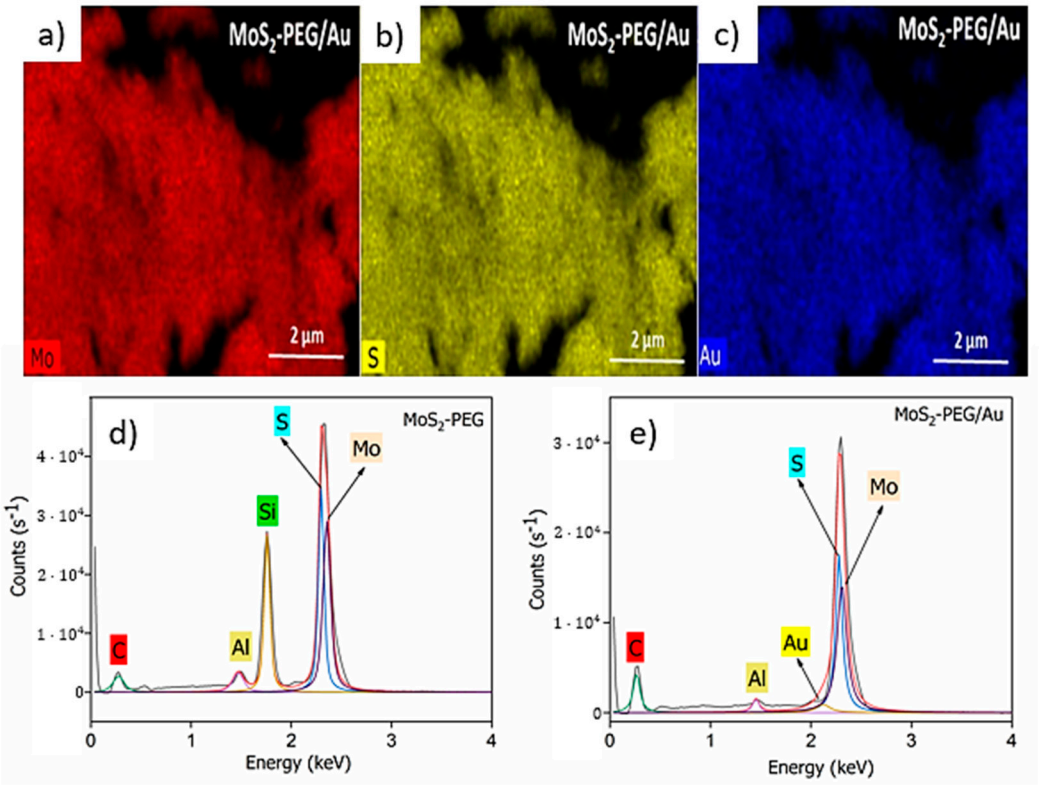


**Figure 3.** (**a**–**c**) Corresponding $MoS_2$-PEG/Au EDS mapping with Mo, S and Au elements. EDS spectrum of (**d**) $MoS_2$-PEG and (**e**) $MoS_2$-PEG/Au.

The FTIR spectrum (Figure 4a) showed the main bands related to the presence of $MoS_2$: 826.4 and 931.5 $cm^{-1}$ [16,37]. The band at 826.4 $cm^{-1}$ represents the stretching mode band of the Mo=O bond. Previous studies reported that when in contact with air, the surface of $MoS_2$ can be partially oxidized and contains adsorbed water, Mo=O groups, sulfate and thiosulfate anions, among others [16,37–39]. At 931.5 $cm^{-1}$, the band originating from the vibrational mode is characteristic of S-S bond [35]. The contribution of PEG begins to appear at 1083.5 $cm^{-1}$, where the intense and sharp band points out to the C–O stretching mode, and at 1427.9 $cm^{-1}$, with less intense but even strong band from the bending mode vibration of C–H. At, 2880.8 $cm^{-1}$, a discrete band is showed from the weak stretching mode vibration of C–H. The results confirm that PEG acts as a wrapper on $MoS_2$ nanoparticles [16,40–42]. As well the weak bands at 3021. 4 and 3179.1 $cm^{-1}$ as the intense bands at 3616.5 and 3715 $cm^{-1}$ correspond to the stretching mode of the inter and intramolecular hydrogen bonds and of the hydroxyl adsorbed from the atmosphere [40–43]. No significant changes were observed in the $MoS_2$-PEG/Au spectrum related to $MoS_2$-PEG, so it was suppressed in this work. For the $MoS_2$-PEG nanomaterial, Raman spectroscopy (Figure 4b) generated the characteristic bands of $MoS_2$ (at 371.5 and 462.8 $cm^{-1}$) assigned to the $E_{2g}$ and $A_{1g}$ vibrational modes, respectively. Such modes, in turn, correspond to the $E_{2g}$ (in-plane) vibrations of sulfur and molybdenum atoms, and to the $A_{1g}$ (out-of-plane) vibrations of them [41]. In the regions of low frequency in Raman (from 329.4 $cm^{-1}$), bands connected to vibrational modes of flexion between C–O and C–O–C were found, as well as low or medium PEG backbone vibrations. The band at 659.3 $cm^{-1}$ is also derived from the

C–C vibration of the PEG skeleton, as well as the intense band at 817.2 $cm^{-1}$ [42,44,45]. The band at 992.7 $cm^{-1}$ refers to the stretching and bending mode of the O–H bonds and the stretching of the C-C bonds, which is well defined and more intense for primary alcohols, as is the case with PEG [34,46–49]. The $MoS_2$-PEG/Au hybrid presented the same bands as the $MoS_2$-PEG, but with the additional band at 1493.0 $cm^{-1}$ ascribed to γ(C–C) from PEG which was intensified due the presence of gold nanostructures [50].

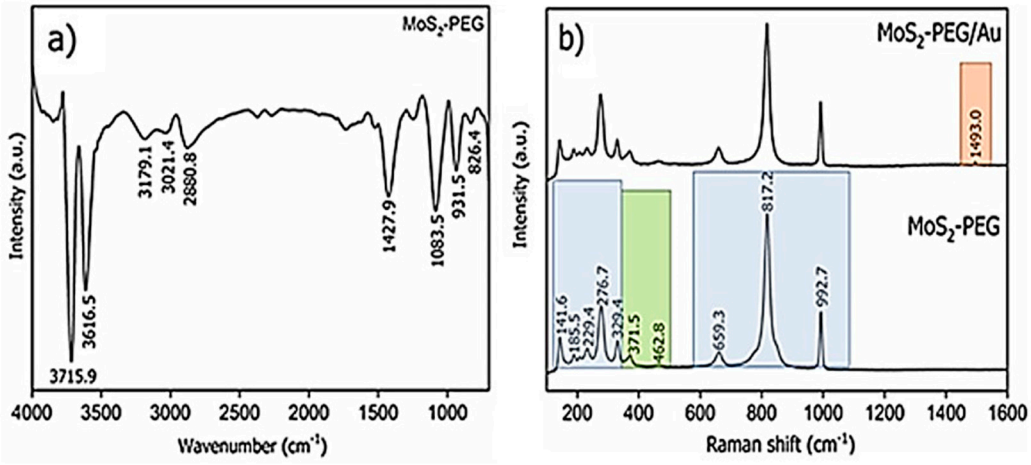


**Figure 4.** FTIR spectrum (**a**) of $MoS_2$-PEG and Raman spectra (**b**) of $MoS_2$-PEG (in black) and $MoS_2$-PEG/Au. Characteristic bands regions referring to $MoS_2$ (in green), PEG (in blue) and Au (in light red) were highlighted.

The surface chemical characterization of the produced nanomaterials was performed by XPS. As shown in the survey spectra, Figure 5a, both $MoS_2$-PEG and $MoS_2$-PEG/Au samples exhibit the elemental Mo, S components as well as carbon and oxygen peaks. The Au4f peak was under the detection limit for $MoS_2$-PEG/Au, suggesting that Au has been covered by the other elements. Figure 5b shows the C1s peak, indicating that the amount of carbon has increased five times after $MoS_2$-PEG/Au synthesis, especially related to the C–O–C, C–OH and C–C species. The O1s peak for $MoS_2$-PEG, see Figure 5c, exhibits a peak at 532.6 eV attributed to O–C, perfectly in line with the presence of PEG [51]. $MoS_2$-PEG/Au shows, besides the O–C bond, a feature at 531 eV which can be attribute to a metal oxide (e.g., $MoO_3$), for that sample. By examination of the Mo3d and S2p doublets of $MoS_2$-PEG, the bottom spectra of Figure 5d,e, respectively, where it is possible to conclude that the $MoS_2$ synthesis was successful. Peaks are very narrow as expected for a crystalline sample and the main peaks, $Mo^{4+}$ $3d_{5/2}$ at 229.5 eV and $S^{2-}$ $2p_{3/2}$ at 162.4 eV agree well with the binding energies found by other authors [52]. Besides that, only a very low contribution of $Mo^{6+}$ attributed to molybdenum oxide and a broad (and low) S2p feature at ~169 eV associated with sulfate ($S^{6+}$) species were observed. The synthesis with AuNPs, which involved bath ultrasound and thermal treatment in air, has importantly modified the surface near region of the sample. Now the Mo $3d_{3/2}$, $3d_{5/2}$ and S $2p_{1/2}$, $2p_{3/2}$ doublets are highly attenuated at the $MoS_2$ binding energy positions, the Mo3d peaks were shifted to higher binding energies, where it can conclude that the surface has been oxidized. Two $Mo3d_{5/2}$ peaks with binding energies of 232.6 eV and 233.6 eV are assigned to molybdenum oxide ($MoO_3$) and molybdate species, respectively. The same occurs to S2p, it shrinks for $MoS_2$, and a sulfur doublet shows up at higher binding energy. The $S2p_{3/2}$ line appearing at 169.6 eV is attributed to $S^{6+}$ in sulfates $(SO_4)^2$, which can be explained by either $MoO_2(SO_4)$ or $Mo(SO_4)_3$ formation at the surface of $MoS_2$. Moreover, it was observed some sulfur loss at the surface near region, which may be due to the formation of volatile sulfur compounds during heat treatment.

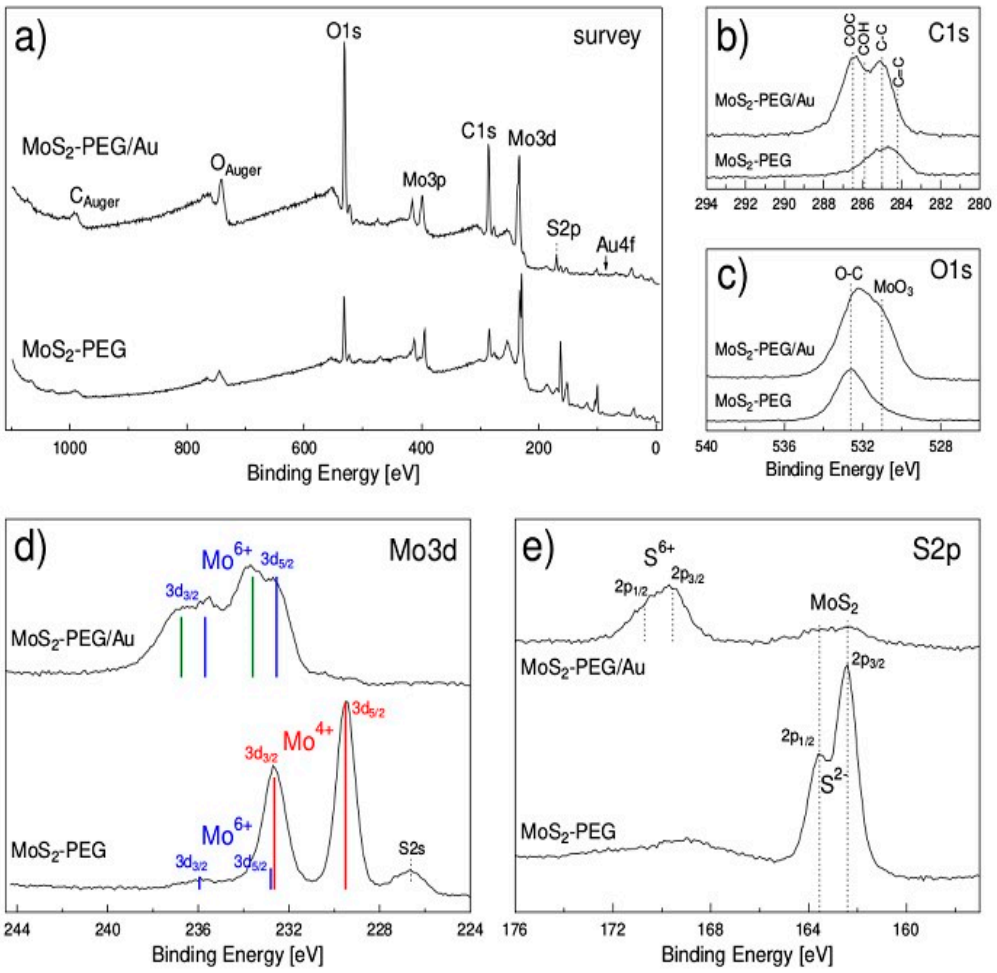


**Figure 5.** X-ray photoelectron spectra of $MoS_2$-PEG and $MoS_2$-PEG/Au samples: survey (**a**), C1s (**b**), O1s (**c**), Mo3d (**d**) and S2p (**e**).

Before the capacitance measurements, the electrical characteristics for $MoS_2$-PEG and $MoS_2$-PEG/Au hybrid microspheres were evaluated by sheet resistance, resistivity and conductivity measurements using the four-point probe technique. As shown in Table 1, the two composites exhibit low electrical conductivity. However, as expected, the incorporation of AuNPs in $MoS_2$-PEG significantly decreased the resistivity of the hybrid system. The best electrical conductivity of the $MoS_2$-PEG/Au nanostructures can be associated with junctions between Au nanoparticles in which the electrons are transferred more easily [53]. Additionally, the sulfur atoms over the outer layer of the $MoS_2$ structure are suitable for the formation of strong Au-S bonds, which improves the charge transfer between sulfur and AuNPs [54,55].

**Table 1.** Electric properties of the $MoS_2$-PEG and $MoS_2$-PEG/Au nanostructures.

| | **Samples** | |
|---|---|---|
| **Electrical Parameters** | **$MoS_2$-PEG** | **$MoS_2$-PEG/Au** |
| Sheet resistance ($k\Omega\ sq^{-1}$) | 671.4 | 218.1 |
| Resistivity ($\Omega$ m) | 1342.7 | 436.2 |
| Conductivity ($10^{-6}$ S $cm^{-1}$) | 7.4 | 22.9 |

Cyclic voltammetry (CV) measurements were performed to evaluate the charge storage capacity of both materials. Figure 6a–d shows the cyclic voltammograms obtained with (a) $MoS_2$-PEG and (c) $MoS_2$-PEG/Au electrodes (geometric area = 3.1 $mm^2$) in 1.0 M $Na_2SO_4$

electrolyte solution over a potential range of −0.2 to 0.4 V at different scan rates. The current signal at the CV curves measured with both electrode materials increases with the corresponding scan rate and the voltammograms show a nearly rectangular aspect, suggesting the charging current is the dominant signal due to reversible adsorption of electrolyte ions on the surface of electrodes. The pattern of specific capacitance decreases for both electrodes (Figure 6b–d) as the scanning rate increases, which can be attributed to lower interactions between electrolyte ions and active sites of the electrode at higher scan rates [56] and as expect the best capacitive results was achieved at 1 mV $s^{-1}$, being 181 F $g^{-1}$ and 96 F $g^{-1}$ for $MoS_2$-PEG and $MoS_2$-PEG/Au, respectively.

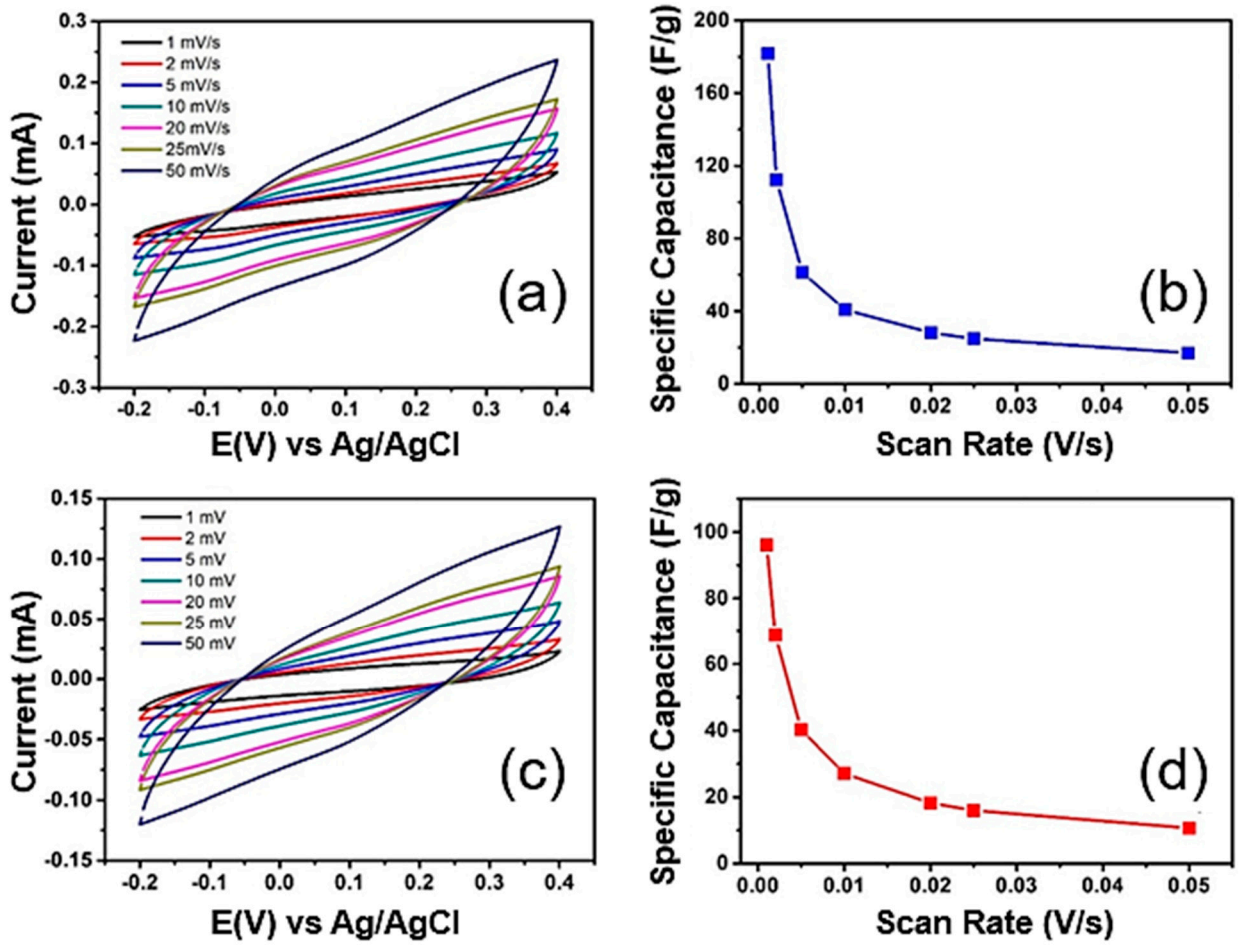


**Figure 6.** Cyclic voltammograms recorded with (**a**) $MoS_2$-PEG and (**c**) $MoS_2$-PEG/Au electrodes at different scan rates in 1.0 M $Na_2SO_4$ electrolyte solution and their respective profiles of specific capacitance (**b**,**d**).

The low capacitance of $MoS_2$-PEG/Au compared to $MoS_2$-PEG was an unexpected fact, however when observing the values of the contact angle measurements of $MoS_2$-PEG and $MoS_2$-PEG/Au electrodes, Table 2, it is verified that the coating $MoS_2$-PEG on the graphite sheet surface electrode presents greater wettability than $MoS_2$-PEG/Au electrode. This fact may be related to the low electroactive area of the $MoS_2$-PEG/Au electrode due to its lower wettability, not allowing the effective access of the electrolyte in the specific electroactive area [57].

**Table 2.** Values of contact angle of graphite sheet, $MoS_2$-PEG and $MoS_2$-PEG/Au nanosheets surfaces.

| Materials | Contact Angle (°) |
|---|---|
| Graphite (substrate) | 58.1 ± 3.9 |
| $MoS_2$-PEG | 30.7 ± 3.4 |
| $MoS_2$-PEG/Au | 37.1 ± 2.1 |

The electrochemical impedance spectroscopy (EIS) technique is an important tool for evaluating the behavior of electrode material at the interface electrolyte-electrode [58]. To examine the performance with both electrode materials, the impedance was measured at 1 MHz to 0.040 Hz at +0.2 V vs. Ag/AgCl with an AC amplitude of 10 mV in a solution containing both $[Fe(CN)_6]^{3-/4-}$ redox couple 2 mM in KCl 0.2 M. The Nyquist plot is a plot of the real part of impedance ($Z'$) vs. imaginary part of impedance ($-Z''$). Figure 7 shows the Nyquist plots for both electrodes. At the highest frequency range, the value at the real axis corresponds to the equivalent series resistance (ESR) and represents the contribution of the electrolyte resistance and the intrinsic resistance of the electrode material. As both electrodes are in the same electrolyte, the ERS reflects the difference in the electrode material.

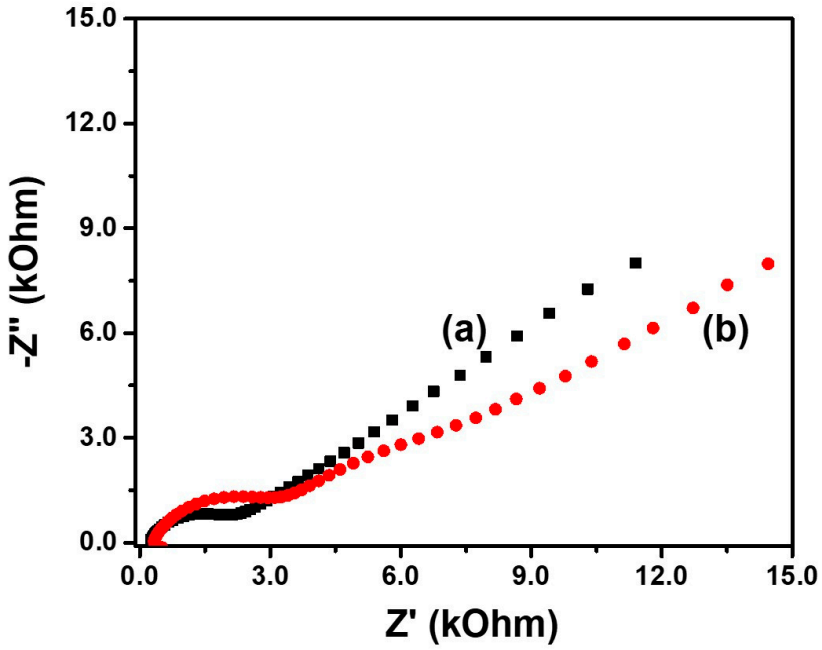


**Figure 7.** Nyquist plots of $MoS_2$-PEG (**a**) and $MoS_2$-PEG/Au (**b**) electrodes measured with $[Fe(CN)_6]^{3-}/[Fe(CN)_6]^{4-}$ 2 mM in KCl 0.1 M electrolyte.

As a comparison, the $MoS_2$-PEG electrode shows an ERS value of 256.4 Ω while $MoS_2$-PEG/Au presents a higher value 339.2 Ω, which can justify the better capacitive performance of the $MoS_2$-PEG electrode. The charge transfer resistance, which is measured from the semi-circle along the real axis from high to medium frequency is also lower in the $MoS_2$-PEG electrode than in the $MoS_2$-PEG/Au one. At low frequency, the Nyquist plots showed a linear range with a slope of near 45°, known as Warburg resistance, where the frequency signal depends on the ion transportation in the electrolyte [57]. The examination of the curves at low frequency shows a smaller Warburg region for the $MoS_2$-PEG electrode, suggesting a lower ion diffusion resistance in the structure of the electrode [59] while impedance performance of the $MoS_2$-PEG/Au electrode shift along the $x$-axis toward more resistive values. Therefore, the better charge transmission and the ion diffusion through the electrode material structure help to explain the higher capacitance of the $MoS_2$-PEG electrode.

The potential cytotoxicity of a given nanomaterial is a prerequisite for biomedical applications. In this study we assessed whether $MoS_2$-PEG or $MoS_2$-PEG/Au could be able to promote reduction of cellular viability in normal and tumoral cells under four different concentrations. The Green Monkey Kidney cell line VeroCCL-81 was used as non-tumoral model and the results applying $MoS_2$-PEG showed discrete cellular viability reduction after 24 h when exposed to 10 μg/mL (2.1 ± 0.2)% and 5 μg/mL (5.2 ± 0.1)%, respectively, as shown in Figure 8a. On the other hand, cells exposed to $MoS_2$PEG/Au demonstrated decreased cellular viability in all concentrations tested, such as (12.2 ± 0.3)% for 100 μg/mL, (19.9 ± 0.9)% for 50 μg/mL, (14.4 ± 0.4)% for 10 μg/mL and (2.5 ± 0.1)% for 5 μg/mL, respectively, compared to 65.5% ± 0.1% of the death control cells. After 48 h no cellular viability reduction was observed for cells exposed to $MoS_2$-PEG and smaller decrease of cellular viability was observed in cells exposed to $MoS_2$-PEG/Au at 100 μg/mL (3.2 ± 0.1)%, 50 μg/mL (5.5 ± 0.2)%, 10 μg/mL (5.0 ± 0.1)% and 5 μg/mL (6.9 ± 0.1)%, respectively, as shown in Figure 8c,d, suggesting a recovery of the cells in a time-dependent manner. Even though good dispersion in water small aggregations were observed over the cells as highlighted in Supporting information Figure S4.

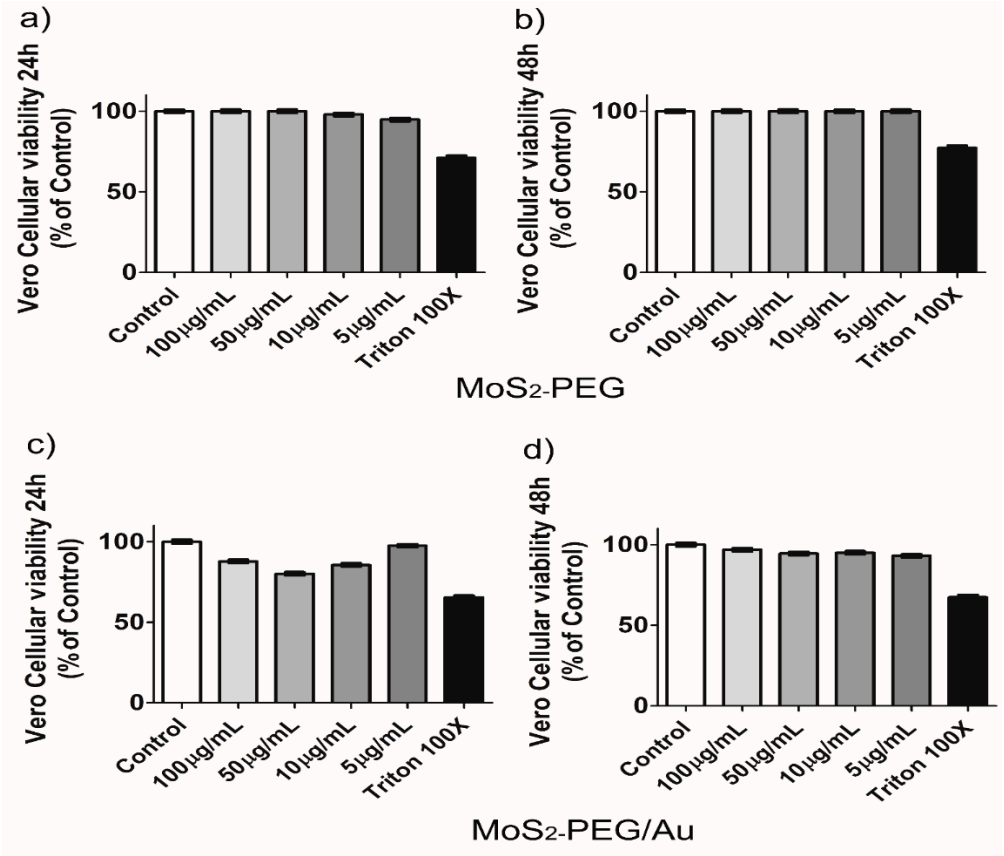


**Figure 8.** Vero cellular viability after 24 h and 48 h. Panels (**a**–**d**) show the percentage of Vero cellular viability exposed to different concentrations of $MoS_2$-PEG and $MoS_2$-PEG/Au. Results of 2 independent experiments in triplicate. (Mean ± SD).

To study the effects of $MoS_2$-PEG and $MoS_2$-PEG/Au in the cellular viability of tumoral cells, the human squamous carcinoma A431 cell line and the human pharynx carcinoma FaDU cell line were used. For A431 cells no difference in the percentage of cellular viability was observed for $MoS_2$-PEG in 24 h, as shown in Figure 9a. For 48 h there were a small decrease of the cellular viability with 100 μg/mL (5.2 ± 0.2)% and 50 μg/mL (5.8 ± 0.3)%, respectively, as observed in panel (b). A similar result was found when these cells were exposed to $MoS_2$-PEG/Au at 48 h showing (3.2 ± 0.1)% decreasing for 100 μg/mL and

(4.2 ± 0.2)% for 50 μg/mL, respectively, as shown in panels (c) and (d). No alterations in the cellular morphology were observed as shown in Supporting information Figure S5.

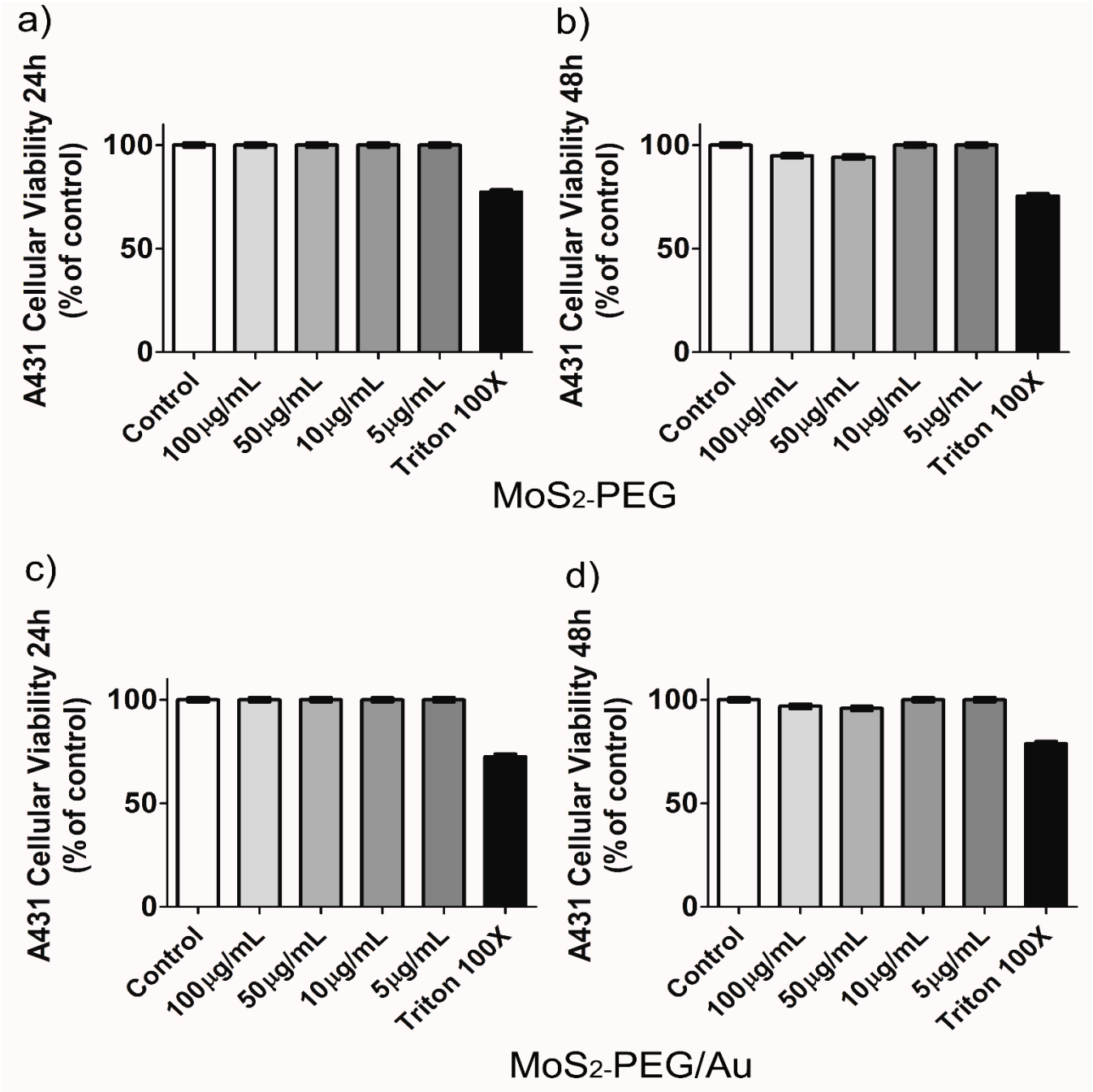


**Figure 9.** A431 cellular viability. Panels (**a**–**d**) show the percentage of cellular viability of these cells exposed to different concentrations of $MoS_2$-PEG and $MoS_2$-PEG/Au. Results representative of 2 independent experiments in triplicate. (Mean ± SD).

Another tumoral model was used and $MoS_2$-PEG showed a decrease of 3.8 ± 0.3% for 100 μg/mL and (11.8 ± 0.2)% for 50 μg/mL at 24 h, as shown in Figure 10a. At 48 h there was only (2.4 ± 0.1)% for 50 μg/mL, suggesting a recovery of these cells in a time-dependent manner and a decrease of (7.3 ± 0.2)% was noticed for 5 μg/mL as shown in panel (b). For $MoS_2$-PEG/Au the most pronounced cellular viability decreasing were observed for 100 μg/mL (6.5 ± 0.9)% and 50 μg/mL (11.61 ± 0.12)% at 48 h, as shown in panels (c) and (d). After contact with both nanomaterials FaDU cells demonstrated morphological

changing when compared to control cells, as shown in Supporting information Figure S6. It is possible that these cells may present, somehow, plasma membrane reaction when in contact with charged materials, by promoting shape alterations. Then, due to the differences observed in their shapes and the decreasing of cellular viability the effect of 100 μg/mL of $MoS_2$-PEG/Au in the number and shape of their nuclei were assessed by Hoechst 33,342 nuclear staining. Interestingly, no differences were observed neither in nuclei number nor in nuclei morphology even at the highest concentration applied, when compared to control cells as shown in Figure 11.

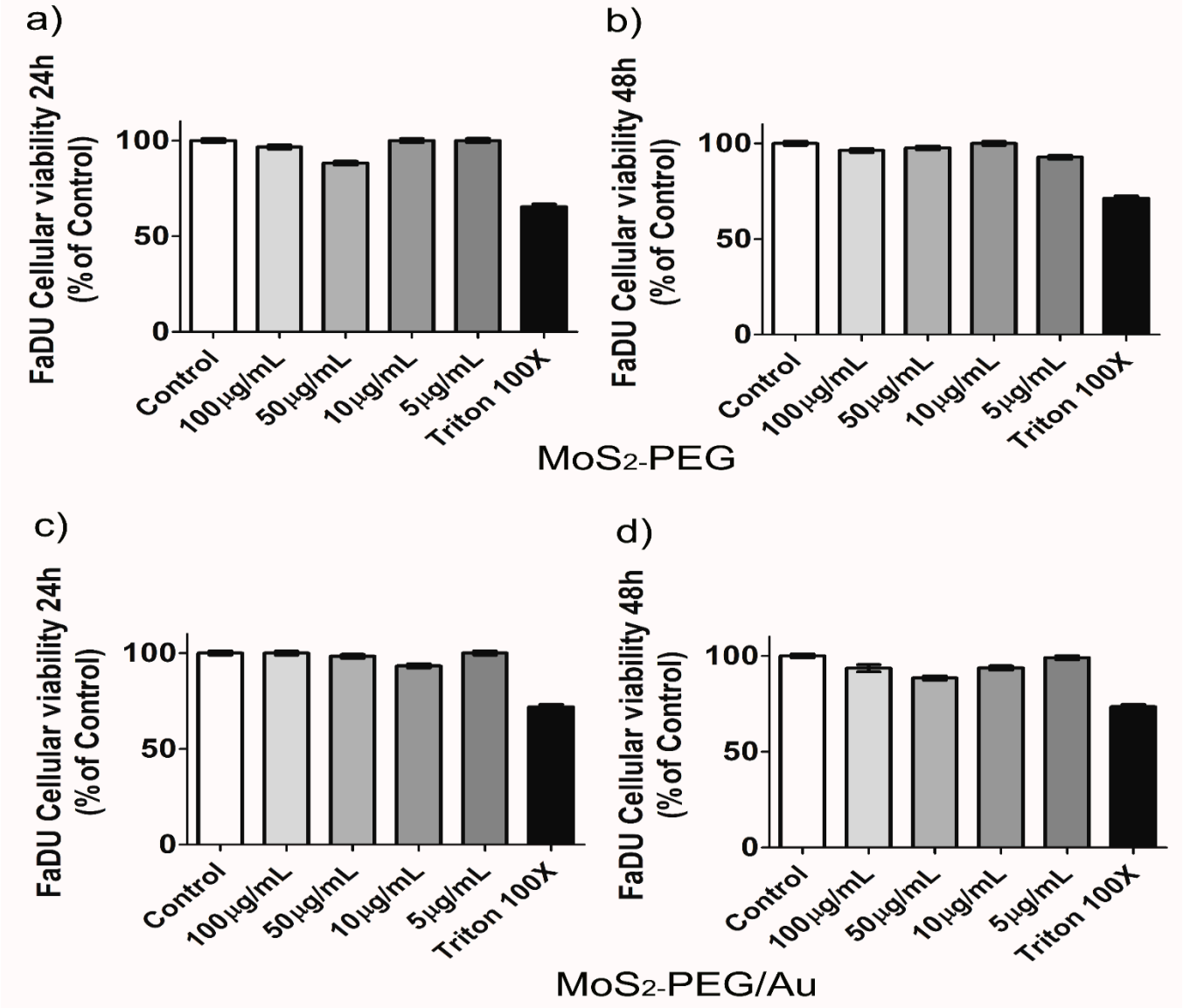


**Figure 10.** FaDU cellular viability. Panels (**a**–**d**) show the percentage of cellular viability of these cells exposed to different concentrations of $MoS_2$-PEG and $MoS_2$-PEG/Au. Results representative of 2 independent experiments in triplicate. (Mean ± SD).

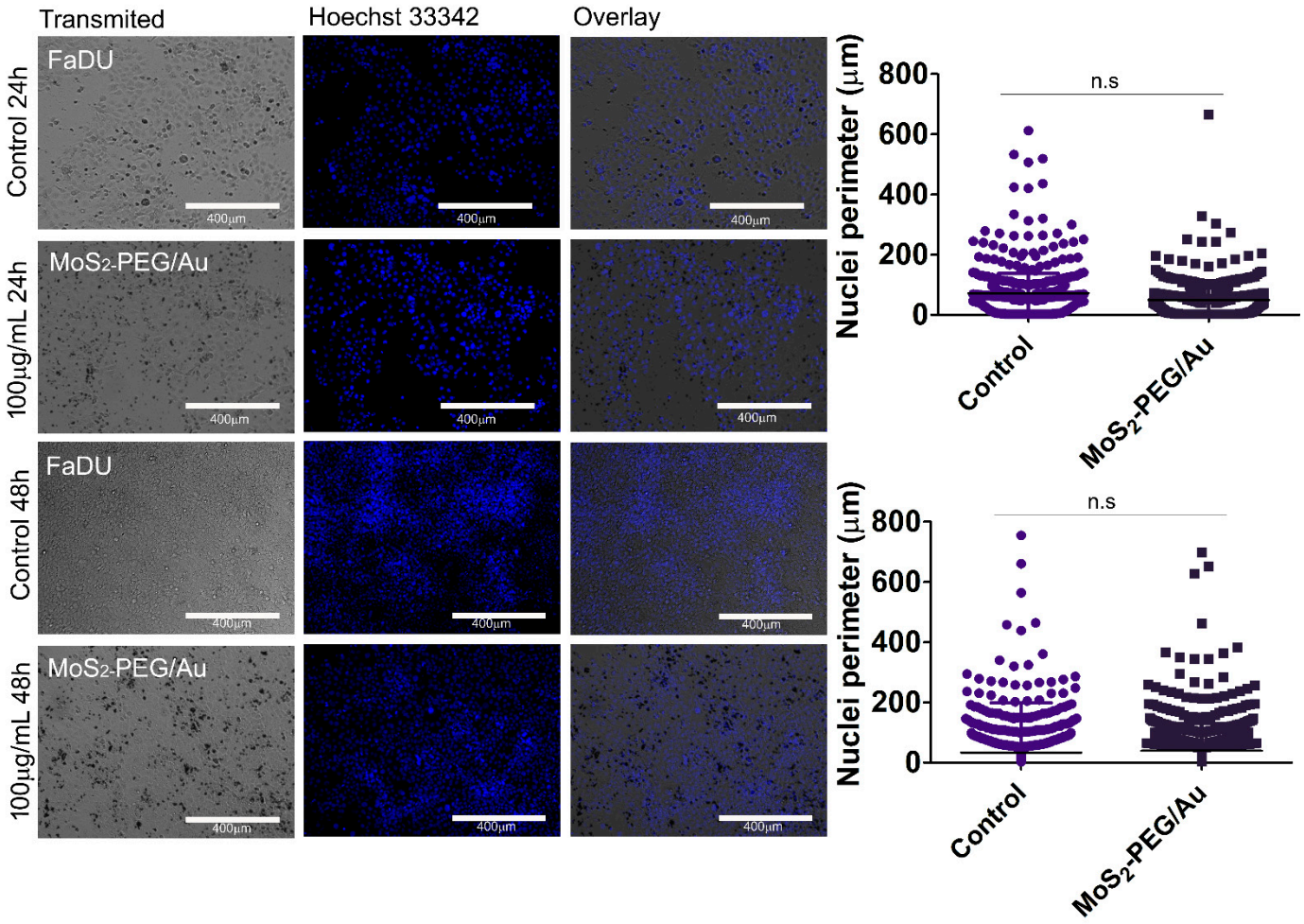


**Figure 11.** FaDU nuclei integrity. Representative fluorescent image of FaDU cells exposed to 100 µg/mL of $MoS_2$-PEG/Au. Nuclei were stained with Hoechst 33,342. Data from 2 replicates (n.s = no significant). Bar scale = 400 µm and objective of 10×.

Our results demonstrated that both nanomaterials are biocompatible in normal cells, as well as in tumoral cells. Despite the high concentrations applied, for instance, 100 µg/mL and 50 µg/mL the cellular viability was kept above 80%. Moreover, at 48 h of contact with $MoS_2$-PEG and $MoS_2$-PEG/Au all cell lines presented very low damage what suggests the safety of these nanomaterials in vitro. Gold nanoparticles have been largely studied in biomedicine due to their well-known biocompatibility [60]. It seems that FaDU cell line changes its shape in contact with both $MoS_2$-PEG and $MoS_2$-PEG/Au. Nonetheless, this change in morphology did not alter cellular viability or nuclear number as demonstrated in Figure 11, corroborating the safety of $MoS_2$-PEG/Au. Although both nanomaterials exhibited good dispersion in water they agglomerated in culture medium, maybe due to the presence of protein and salt. However, $MoS_2$-PEG and $MoS_2$-PEG/Au structures were able to adsorb in the cellular membranes and it is possible that a small amount of these nanomaterials carried into the cells which explains the alterations in cellular viability percentages. It was already shown that 2D $MoS_2$ nanoparticles do not promote deleterious effects in cellular viability or induce genetic defects in HEK293f cells [20]. In this way, our data suggest the same behavior in other cellular models. Since neither $MoS_2$-PEG and $MoS_2$-PEG/Au themselves decrease cellular viability, they can be functionalized for theranostic purposes. We believe that $MoS_2$-PEG/Au may possess potential application as a platform for theranostic, especially for cancer screening and photothermal therapy, because transition-metal dichalcogenides also enhance fluorescence through FRET and $MoS_2$

nanosheets coated with folic acid had demonstrated efficient detection of miRNA-21 expression in a unique MCF-7 and HeLa cancer cells lines, working as a fluorescent nanoprobe. Based on the lack of cellular injuries demonstrated by our data both nanocomposites could have their surfaces modified to improve their dispersibility in aqueous solution. As an example, $MoS_2$-PEG could be investigated as a new contrast agent for radiological imaging, and $MoS_2$-PEG/Au could be functionalized to promote drug-delivery. The carefully physicochemical and biological characterizations of nanomaterials for biomedical applications are the first steps for a such proposal [61], and our work provides data enough to indicate $MoS_2$-PEG/Au for these purposes. Then, this initial study paves the way for other works in nanobiomedicine, for instance by incorporating dyes and/or biomolecules to $MoS_2$-PEG/Au by taking advantages of the excellent optical properties of AuNPs and $MoS_2$ as well.

## 4. Conclusions

$MoS_2$-PEG and $MoS_2$-PEG/Au were successfully synthesized and widely characterized with different physicochemical techniques. By using TEM and SEM, it was possible to verify hierarchical flower-like structures, with a lateral size of up to 400 nm. Through the EDS and XPS studies, it was also observed that AuNPs were distributed throughout the material. $MoS_2$-PEG/Au sample showed a lower capacitance value compared to $MoS_2$-PEG; this fact may be associated with the low wettability of this electrode as observed in its contact angle. In this case, the presence of AuNPs could be related to increase the $MoS_2$-PEG hydrophobicity, allowing only partial contact between the electrode and the electrolyte. However, in both cases the produced samples showed chemical stability and biocompatibility, due to the cell viability achieved above 80% for different times. Thus, its potential use as multifunctional nanomaterial for theranostic applications is an important subject that needs to be better explored.

**Supplementary Materials:** The following supporting information can be downloaded at: https://www.mdpi.com/article/10.3390/nano12122053/s1, Figure S1: (a) TEM images of Au nanoparticles (AuNPs) and (b) UV-Vis of Au nanoparticles (AuNPs) suspension.; Figure S2. Image tablets or electrodes MoS2-PEG (a,c), and MoS2-PEG/Au (b,d).; Figure S3. (A) Electrochemical cell design: (a,b) plexiglass pieces; (c) auxiliary electrode; (d) Ag/AgCl reference electrode; (e) working electrode.; Figure S4: Vero cellular morphology. Representative Images show Vero cells exposed to four concentrations of these nanomaterials at 24 h and 48 h. (Bar scale = 400 µm, transmitted image in 10× objective).; Figure S5: A431 cellular morphology. Representative Images show A431 cells exposed to four concentrations of these nanomaterials at 24 h and 48 h. (Bar scale = 400 µm, transmitted image in 10× objective).; Figure S6: FaDU cellular morphology. Representative Images show FaDU cells exposed to four concentrations of these nanomaterials at 24 h and 48 h. (Bar scale = 400 µm, transmitted image in 10× objective). References [62–65] are cited in the supplementary materials.

**Author Contributions:** T.R.S.M., W.M.S., H.R. and J.T.-T. contributed to the conceptualization, methodology, measuring campaign, literature research, project administration, data interpretation, data analysis, validation, formal analysis, resources, investigation, figures, study design, supervision and writing. All authors contributed to the methodology, resources, data interpretation, validation, formal analysis, investigation, figures and writing. A.P.G., J.M.B., A.G.T.L., N.C.O.S., J.J.P., P.S.G., R.M.P., L.M.A., S.H.D., contributed to the measuring campaign, literature research, data interpretation, data analysis, validation, formal analysis, resources, investigation, figures, study design and writing. All authors have read and agreed to the published version of the manuscript.

**Funding:** This research was sponsored by Mackenzie Research Fund (MackPesquisa, Project No. 181009), National Council for Scientific and Technological Development (CNPq), Coordination for the Improvement of Higher Education Personnel-Brazil (CAPES), and the Universidad de Monterrey.

**Institutional Review Board Statement:** Not applicable.

**Informed Consent Statement:** Not applicable.

**Data Availability Statement:** Data presented in this article are available at request from the corresponding author.

**Acknowledgments:** The authors would like to thank Universidad de Monterrey, Mexico, and Professor Flávio Guimarães da Fonseca from Laboratório de Virologia Básica e Aplicada da Universidade Federal de Minas Gerais, for the use of his facilities, Brazil National Council for Scientific and Technological Development (CNPq), and Coordination for the Improvement of Higher Education Personnel-Brazil (CAPES) and MackPesquisa.

**Conflicts of Interest:** The authors declare no conflict of interest or financial intention.

## References

1. Silva, W.M.; Ribeiro, H.; Taha-Tijerina, J.J. Potential Production of Theranostic Boron Nitride Nanotubes (64Cu-BNNTs) Radiolabeled by Neutron Capture. *Nanomaterials* **2021**, *11*, 2907. [CrossRef] [PubMed]
2. Yoon, J.; Lim, J.; Shin, M.; Lee, S.-N.; Choi, J.-W. Graphene/MoS2 Nanohybrid for Biosensors. *Materials* **2021**, *14*, 518. [CrossRef] [PubMed]
3. Wong, B.S.; Yoong, S.L.; Jagusiak, A.; Panczyk, T.; Ho, H.K.; Ang, W.H.; Pastorin, G. Carbon Nanotubes for Delivery of Small Molecule Drugs. *Adv. Drug Deliv. Rev.* **2013**, *65*, 1964–2015. [CrossRef] [PubMed]
4. Kim, N.Y.; Blake, S.; De, D.; Ouyang, J.; Shi, J.; Kong, N. Two-Dimensional Nanosheet-Based Photonic Nanomedicine for Combined Gene and Photothermal Therapy. *Front. Pharmacol.* **2020**, *10*, 1–14. [CrossRef]
5. Ma, B.; Bianco, A. Recent Advances in 2D Material-Mediated Immuno-Combined Cancer Therapy. *Small* **2021**, *17*, 2102557. [CrossRef]
6. de Melo-Diogo, D.; Pais-Silva, C.; Dias, D.R.; Moreira, A.F.; Correia, I.J. Strategies to Improve Cancer Photothermal Therapy Mediated by Nanomaterials. *Adv. Healthc. Mater.* **2017**, *6*, 1700073. [CrossRef]
7. Jain, P.K.; El-Sayed, I.H.; El-Sayed, M.A. Au Nanoparticles Target Cancer. *Nano Today* **2007**, *2*, 18–29. [CrossRef]
8. Tian, B.; Wang, C.; Zhang, S.; Feng, L.; Liu, Z. Photothermally Enhanced Photodynamic Therapy Delivered by Nano-Graphene Oxide. *ACS Nano* **2011**, *5*, 7000–7009. [CrossRef]
9. Robinson, J.T.; Tabakman, S.M.; Liang, Y.; Wang, H.; Sanchez Casalongue, H.; Vinh, D.; Dai, H. Ultrasmall Reduced Graphene Oxide with High Near-Infrared Absorbance for Photothermal Therapy. *J. Am. Chem. Soc.* **2011**, *133*, 6825–6831. [CrossRef]
10. Li, L.; Li, J.; Shi, Y.; Du, P.; Zhang, Z.; Liu, T.; Zhang, R.; Liu, Z. On-Demand Biodegradable Boron Nitride Nanoparticles for Treating Triple Negative Breast Cancer with Boron Neutron Capture Therapy. *ACS Nano* **2019**, *13*, 13843–13852. [CrossRef]
11. Qian, X.; Gu, Z.; Chen, Y. Two-Dimensional Black Phosphorus Nanosheets for Theranostic Nanomedicine. *Mater. Horiz.* **2017**, *4*, 800–816. [CrossRef]
12. Cheng, L.; Liu, J.; Gu, X.; Gong, H.; Shi, X.; Liu, T.; Wang, C.; Wang, X.; Liu, G.; Xing, H.; et al. PEGylated WS2 Nanosheets as a Multifunctional Theranostic Agent for in Vivo Dual-Modal CT/Photoacoustic Imaging Guided Photothermal Therapy. *Adv. Mater.* **2014**, *26*, 1886–1893. [CrossRef]
13. Wang, J.; Sui, L.; Huang, J.; Miao, L.; Nie, Y.; Wang, K.; Yang, Z.; Huang, Q.; Gong, X.; Nan, Y.; et al. MoS2-Based Nanostructures for Cancer Diagnosis and Therapy. *Bioact. Mater.* **2021**, *6*, 4209–4242. [CrossRef]
14. Lu, J.; Chen, M.; Dong, L.; Cai, L.; Zhao, M.; Wang, Q.; Li, J. Molybdenum Disulfide Nanosheets: From Exfoliation Preparation to Biosensing and Cancer Therapy Applications. *Colloids Surf. B Biointerfaces* **2020**, *194*, 111162. [CrossRef]
15. Xu, M.; Zhang, K.; Liu, Y.; Wang, J.; Wang, K.; Zhang, Y. Multifunctional MoS2 Nanosheets with Au NPs Grown in Situ for Synergistic Chemo-Photothermal Therapy. *Colloids Surf. B Biointerfaces* **2019**, *184*, 110551. [CrossRef]
16. Feng, W.; Chen, L.; Qin, M.; Zhou, X.; Zhang, Q.; Miao, Y.; Qiu, K.; Zhang, Y.; He, C. Flower-like PEGylated MoS2 Nanoflakes for near-Infrared Photothermal Cancer Therapy. *Sci. Rep.* **2015**, *5*, 17422. [CrossRef]
17. Wang, X.; Chang, J.; Wu, C. MoS2-Based Biomaterials for Cancer Therapy. In *Biomaterials in Translational Medicine*; Elsevier: Amsterdam, The Netherlands, 2019; pp. 141–161. ISBN 9780128134771.
18. Ribeiro, H.; Trigueiro, J.P.C.; Silva, W.M.; Woellner, C.F.; Owuor, P.S.; Cristian Chipara, A.; Lopes, M.C.; Tiwary, C.S.; Pedrotti, J.J.; Villegas Salvatierra, R.; et al. Hybrid MoS2/h-BN Nanofillers As Synergic Heat Dissipation and Reinforcement Additives in Epoxy Nanostructures. *ACS Appl. Mater. Interfaces* **2019**, *11*, 24485–24492. [CrossRef]
19. Ribeiro, H.; Trigueiro, J.P.C.; Owuor, P.S.; Machado, L.D.; Woellner, C.F.; Pedrotti, J.J.; Jaques, Y.M.; Kosolwattana, S.; Chipara, A.; Silva, W.M.; et al. Hybrid 2D Nanostructures for Mechanical Reinforcement and Thermal Conductivity Enhancement in Polymer Composites. *Compos. Sci. Technol.* **2018**, *159*, 103–110. [CrossRef]
20. Appel, J.H.; Li, D.O.; Podlevsky, J.D.; Debnath, A.; Green, A.A.; Wang, Q.H.; Chae, J. Low Cytotoxicity and Genotoxicity of Two-Dimensional MoS2 and WS2. *ACS Biomater. Sci. Eng.* **2016**, *2*, 361–367. [CrossRef]
21. Wang, S.; Li, K.; Chen, Y.; Chen, H.; Ma, M.; Feng, J.; Zhao, Q.; Shi, J. Biocompatible PEGylated MoS2 Nanosheets: Controllable Bottom-up Synthesis and Highly Efficient Photothermal Regression of Tumor. *Biomaterials* **2015**, *39*, 206–217. [CrossRef]
22. Wang, P.; Wang, H.; Zhao, X.; Li, L.; Chen, M.; Cheng, J.; Liu, J.; Li, X. Antibacterial Activity and Cytotoxicity of Novel Silkworm-like Nisin@PEGylated MoS2. *Colloids Surf. B Biointerfaces* **2019**, *183*, 110491. [CrossRef]
23. Liu, T.; Wang, C.; Cui, W.; Gong, H.; Liang, C.; Shi, X.; Li, Z.; Sun, B.; Liu, Z. Combined Photothermal and Photodynamic Therapy Delivered by PEGylated MoS2 Nanosheets. *Nanoscale* **2014**, *6*, 11219–11225. [CrossRef]

24. Wang, J.; Wu, X.; Shen, P.; Wang, J.; Shen, Y.; Shen, Y.; Webster, T.J.; Deng, J. Applications of Inorganic Nanomaterials in Photothermal Therapy Based on Combinational Cancer Treatment. *Int. J. Nanomed.* **2020**, *15*, 1903–1914. [CrossRef]
25. Xu, J.; Gulzar, A.; Liu, Y.; Bi, H.; Gai, S.; Liu, B.; Yang, D.; He, F.; Yang, P. Integration of IR-808 Sensitized Upconversion Nanostructure and MoS2 Nanosheet for 808 Nm NIR Light Triggered Phototherapy and Bioimaging. *Small* **2017**, *13*, 1701841. [CrossRef]
26. Yadav, V.; Roy, S.; Singh, P.; Khan, Z.; Jaiswal, A. 2D MoS2-Based Nanomaterials for Therapeutic, Bioimaging, and Biosensing Applications. *Small* **2019**, *15*, 1803706. [CrossRef]
27. Xie, W.; Gao, Q.; Wang, D.; Guo, Z.; Gao, F.; Wang, X.; Cai, Q.; Feng, S.; Fan, H.; Sun, X.; et al. Doxorubicin-Loaded Fe3O4@MoS2-PEG-2DG Nanocubes as a Theranostic Platform for Magnetic Resonance Imaging-Guided Chemo-Photothermal Therapy of Breast Cancer. *Nano Res.* **2018**, *11*, 2470–2487. [CrossRef]
28. Shi, J.; Zhang, H.; Chen, Z.; Xu, L.; Zhang, Z. A Multi-Functional Nanoplatform for Efficacy Tumor Theranostic Applications. *Asian J. Pharm. Sci.* **2017**, *12*, 235–249. [CrossRef]
29. Reis, D.S.; de Oliveira, V.L.; Silva, M.L.; Paniago, R.M.; Ladeira, L.O.; Andrade, L.M. Gold Nanoparticles Enhance Fluorescence Signals by Flow Cytometry at Low Antibody Concentrations. *J. Mater. Chem. B* **2021**, *9*, 1414–1423. [CrossRef] [PubMed]
30. Liu, L.; Wang, J.; Tan, X.; Pang, X.; You, Q.; Sun, Q.; Tan, F.; Li, N. Photosensitizer Loaded PEG-MoS2-Au Hybrids for CT/NIRF Imaging-Guided Stepwise Photothermal and Photodynamic Therapy. *J. Mater. Chem. B* **2017**, *5*, 2286–2296. [CrossRef]
31. Liu, M.; Zhu, H.; Wang, Y.; Sevencan, C.; Li, B.L. Functionalized MoS2-Based Nanomaterials for Cancer Phototherapy and Other Biomedical Applications. *ACS Mater. Lett.* **2021**, *3*, 462–496. [CrossRef]
32. Zhang, H.; Fan, T.; Chen, W.; Li, Y.; Wang, B. Recent Advances of Two-Dimensional Materials in Smart Drug Delivery Nano-Systems. *Bioact. Mater.* **2020**, *5*, 1071–1086. [CrossRef] [PubMed]
33. Meireles, I.B.D.C.J.; Cipreste, M.F.; Gastelois, P.L.; Macedo, W.A.D.A.; Gomes, D.A.; de Sousa, E.M.B. Synthesis and Characterization of Gold Nanorods Coated by Mesoporous Silica MCM-41 as a Platform for Bioapplication in Photohyperthermia. *Nanotechnology* **2021**, *32*, 505720. [CrossRef] [PubMed]
34. Kumari, S.; Gusain, R.; Kumar, N.; Khatri, O.P. PEG-Mediated Hydrothermal Synthesis of Hierarchical Microspheres of MoS2 Nanosheets and Their Potential for Lubrication Application. *J. Ind. Eng. Chem.* **2016**, *42*, 87–94. [CrossRef]
35. Lalithambika, K.C.; Shanmugapriya, K.; Sriram, S. Photocatalytic Activity of MoS2 Nanoparticles: An Experimental and DFT Analysis. *Appl. Phys. A* **2019**, *125*, 817. [CrossRef]
36. Viet Long, N.; Ohtaki, M.; Yuasa, M.; Yoshida, S.; Kuragaki, T.; Minh Thi, C.; Nogami, M. Synthesis and Self-Assembly of Gold Nanoparticles by Chemically Modified Polyol Methods under Experimental Control. *J. Nanomater.* **2013**, *2013*, 793125. [CrossRef]
37. Maugé, F.; Lamotte, J.; Nesterenko, N.S.; Manoilova, O.; Tsyganenko, A.A. FT-IR Study of Surface Properties of Unsupported MoS2. *Catal. Today* **2001**, *70*, 271–284. [CrossRef]
38. Perumal Veeramalai, C.; Li, F.; Xu, H.; Kim, T.W.; Guo, T. One Pot Hydrothermal Synthesis of Graphene like MoS2 Nanosheets for Application in High Performance Lithium Ion Batteries. *RSC Adv.* **2015**, *5*, 57666–57670. [CrossRef]
39. Ali, G.A.M.; Thalji, M.R.; Soh, W.C.; Algarni, H.; Chong, K.F. One-Step Electrochemical Synthesis of MoS2/Graphene Composite for Supercapacitor Application. *J. Solid State Electrochem.* **2020**, *24*, 25–34. [CrossRef]
40. Liu, T.; Wang, C.; Gu, X.; Gong, H.; Cheng, L.; Shi, X.; Feng, L.; Sun, B.; Liu, Z. Drug Delivery with PEGylated MoS2 Nano-Sheets for Combined Photothermal and Chemotherapy of Cancer. *Adv. Mater.* **2014**, *26*, 3433–3440. [CrossRef]
41. Chen, J.; Xu, Z.; Hu, Y.; Yi, M. PEG-assisted Solvothermal Synthesis of MoS2 Nanosheets with Enhanced Tribological Property. *Lubr. Sci.* **2020**, *32*, 273–282. [CrossRef]
42. Sagitova, E.A.; Prokhorov, K.A.; Nikolaeva, G.Y.; Baimova, A.V.; Pashinin, P.P.; Yarysheva, A.Y.; Mendeleev, D.I. Raman Analysis of Polyethylene Glycols and Polyethylene Oxides. *J. Phys. Conf. Ser.* **2018**, *999*, 012002. [CrossRef]
43. Wang, T.; Liu, W.; Tian, J. Preparation and Characterization of Gold/Poly(Vinyl Alcohol)/MoS2 Intercalation Nanostructure. *J. Mater. Sci. Mater. Electron.* **2004**, *15*, 435–438. [CrossRef]
44. Dinç, C.Ö.; Güner, A. Solid-State Characterization of Poly(Ethylene Glycol) Samples Prepared by Solvent Cast Technique. *Bulg. Chem. Commun.* **2017**, *49*, 14–20.
45. Socrates, G. *Infrared and Raman Characteristic Group Frequencies: Tables and Charts*, 3rd ed.; John Wiley & Sons Ltd.: London, UK, 2001; ISBN 978-0-470-09307-8.
46. León, A.; Reuquen, P.; Garín, C.; Segura, R.; Vargas, P.; Zapata, P.; Orihuela, P. FTIR and Raman Characterization of TiO2 Nanoparticles Coated with Polyethylene Glycol as Carrier for 2-Methoxyestradiol. *Appl. Sci.* **2017**, *7*, 49. [CrossRef]
47. Constantinescu, M.; Dumitrache, L.; Constantinescu, D.; Anghel, E.M.; Popa, V.T.; Stoica, A.; Olteanu, M. Latent Heat Nano Composite Building Materials. *Eur. Polym. J.* **2010**, *46*, 2247–2254. [CrossRef]
48. Kozielski, M.; Mühle, M.; Błaszczak, Z. The Raman Scattering Study of Selected Polyoxyethyleneglycols. *J. Mol. Liq.* **2004**, *111*, 1–5. [CrossRef]
49. Ntakadzeni, M.; Anku, W.W.; Kumar, N.; Govender, P.P.; Reddy, L. PEGylated MoS2 Nanosheets: A Dual Functional Photocatalyst for Photodegradation of Organic Dyes and Photoreduction of Chromium from Aqueous Solution. *Bull. Chem. React. Eng. Catal.* **2019**, *14*, 142. [CrossRef]
50. Tiwari, N. Study of Adsorption Behavior of Aminothiophenols on Gold Nanorods Using Surface-Enhanced Raman Spectroscopy. *J. Nanophotonics* **2011**, *5*, 053513. [CrossRef]

51. López, G.P.; Castner, D.G.; Ratner, B.D. XPS O 1s Binding Energies for Polymers Containing Hydroxyl, Ether, Ketone and Ester Groups. *Surf. Interface Anal.* **1991**, *17*, 267–272. [CrossRef]
52. Syari'ati, A.; Kumar, S.; Zahid, A.; Ali El Yumin, A.; Ye, J.; Rudolf, P. Photoemission Spectroscopy Study of Structural Defects in Molybdenum Disulfide (MoS2) Grown by Chemical Vapor Deposition (CVD). *Chem. Commun.* **2019**, *55*, 10384–10387. [CrossRef]
53. Wang, R.; Chen, C.; Zheng, Y.; Wang, H.; Liu, J.-W.; Yu, S.-H. Structure–Property Relationship of Assembled Nanowire Materials. *Mater. Chem. Front.* **2020**, *4*, 2881–2903. [CrossRef]
54. Polyakov, A.Y.; Yadgarov, L.; Popovitz-Biro, R.; Lebedev, V.A.; Pinkas, I.; Rosentsveig, R.; Feldman, Y.; Goldt, A.E.; Goodilin, E.A.; Tenne, R. Decoration of WS2 Nanotubes and Fullerene-Like MoS2 with Gold Nanoparticles. *J. Phys. Chem. C* **2014**, *118*, 2161–2169. [CrossRef]
55. Vinita; Nirala, N.R.; Prakash, R. One Step Synthesis of AuNPs@MoS2-QDs Composite as a Robust Peroxidase-Mimetic for Instant Unaided Eye Detection of Glucose in Serum, Saliva and Tear. *Sens. Actuators B Chem.* **2018**, *263*, 109–119. [CrossRef]
56. Wang, R.; Li, Q.; Cheng, L.; Li, H.; Wang, B.; Zhao, X.S.; Guo, P. Electrochemical Properties of Manganese Ferrite-Based Supercapacitors in Aqueous Electrolyte: The Effect of Ionic Radius. *Colloids Surf. A Physicochem. Eng. Asp.* **2014**, *457*, 94–99. [CrossRef]
57. Liu, T.; Wang, K.; Chen, Y.; Zhao, S.; Han, Y. Dominant Role of Wettability in Improving the Specific Capacitance. *Green Energy Environ.* **2019**, *4*, 171–179. [CrossRef]
58. Taberna, P.L.; Portet, C.; Simon, P. Electrode Surface Treatment and Electrochemical Impedance Spectroscopy Study on Carbon/Carbon Supercapacitors. *Appl. Phys. A* **2006**, *82*, 639–646. [CrossRef]
59. Yamada, Y.; Sasaki, T.; Tatsuda, N.; Weingarth, D.; Yano, K.; Kötz, R. A Novel Model Electrode for Investigating Ion Transport inside Pores in an Electrical Double-Layer Capacitor: Monodispered Microporous Starburst Carbon Spheres. *Electrochim. Acta* **2012**, *81*, 138–148. [CrossRef]
60. Versiani, A.F.; Andrade, L.M.; Martins, E.M.N.; Scalzo, S.; Geraldo, J.M.; Chaves, C.R.; Ferreira, D.C.; Ladeira, M.; Guatimosim, S.; Ladeira, L.O.; et al. Gold Nanoparticles and Their Applications in Biomedicine. *Future Virol.* **2016**, *11*, 293–309. [CrossRef]
61. Andrade, L.M.; Martins, E.M.N.; Versiani, A.F.; Reis, D.S.; da Fonseca, F.G.; Souza, I.P.d.; Paniago, R.M.; Pereira-Maia, E.; Ladeira, L.O. The Physicochemical and Biological Characterization of a 24-Month-Stored Nanocomplex Based on Gold Nanoparticles Conjugated with Cetuximab Demonstrated Long-Term Stability, EGFR Affinity and Cancer Cell Death Due to Apoptosis. *Mater. Sci. Eng. C* **2020**, *107*, 110203. [CrossRef]
62. Steckiewicz, K.P.; Barcinska, E.; Malankowska, A.; Zauszkiewicz–Pawlak, A.; Nowaczyk, G.; Zaleska-Medynska, A.; Inkielewicz-Stepniak, I. Impact of Gold Nanoparticles Shape on Their Cytotoxicity against Human Osteoblast and Osteosarcoma in in Vitro Model. Evaluation of the Safety of Use and Anti-Cancer Potential. *J. Mater. Sci. Mater. Med.* **2019**, *30*, 22. [CrossRef]
63. Kooij, E.S.; Ahmed, W.; Hellenthal, C.; Zandvliet, H.J.W.; Poelsema, B. From Nanorods to Nanostars: Tuning the Optical Properties of Gold Nanoparticles. *Colloids Surf. A Physicochem. Eng. Asp.* **2012**, *413*, 231–238. [CrossRef]
64. Zhong, X.; Chai, Y.-Q.; Yuan, R. A Novel Strategy for Synthesis of Hollow Gold Nanosphere and Its Application in Electrogenerated Chemiluminescence Glucose Biosensor. *Talanta* **2014**, *128*, 9–14. [CrossRef] [PubMed]
65. Pedrotti, J.J.; Angnes, L.; Gutz, I.G.R. Miniaturized Reference Electrodes with Microporous Polymer Junctions. *Electroanalysis* **1996**, *8*, 673–675. [CrossRef]